



# Observations of XCO<sub>2</sub> and XCH<sub>4</sub> with ground-based high-resolution FTS at Saga, Japan, and comparisons with GOSAT products

H. Ohyama<sup>1,a</sup>, S. Kawakami<sup>1</sup>, T. Tanaka<sup>1,b</sup>, I. Morino<sup>2</sup>, O. Uchino<sup>2</sup>, M. Inoue<sup>2,c</sup>, T. Sakai<sup>3</sup>, T. Nagai<sup>3</sup>, A. Yamazaki<sup>3</sup>, A. Uchiyama<sup>3</sup>, T. Fukamachi<sup>4</sup>, M. Sakashita<sup>4</sup>, T. Kawasaki<sup>4</sup>, T. Akaho<sup>4</sup>, K. Arai<sup>4</sup>, and H. Okumura<sup>4</sup>

<sup>1</sup>Japan Aerospace Exploration Agency, Tsukuba, Japan

<sup>2</sup>National Institute for Environmental Studies, Tsukuba, Japan

<sup>3</sup>Meteorological Research Institute, Tsukuba, Japan

<sup>4</sup>Graduate School of Science and Engineering, Saga University, Saga, Japan

<sup>a</sup>now at: Institute for Space-Earth Environmental Research, Nagoya University, Nagoya, Japan

<sup>b</sup>now at: NASA Ames Research Center, Moffett Field, CA 94035, USA

<sup>c</sup>now at: Department of Biological Environment, Akita Prefectural University, Akita, Japan

Correspondence to: H. Ohyama (hohyama@stelab.nagoya-u.ac.jp)

Received: 15 June 2015 – Published in Atmos. Meas. Tech. Discuss.: 7 August 2015

Revised: 25 November 2015 – Accepted: 30 November 2015 – Published: 17 December 2015

**Abstract.** Solar absorption spectra in the near-infrared region have been continuously acquired with a ground-based (g-b) high-resolution Fourier transform spectrometer (FTS) at Saga, Japan, since July 2011. Column-averaged dry-air mole fractions of greenhouse gases were retrieved from the measured spectra for the period from July 2011 to December 2014. Aircraft measurements of CO<sub>2</sub> and CH<sub>4</sub> for calibrating the g-b FTS data were performed in January 2012 and 2013, and it is found that the g-b FTS and aircraft data agree to within  $\pm 0.2\%$ . The column-averaged dry-air mole fractions of CO<sub>2</sub> and CH<sub>4</sub> (XCO<sub>2</sub> and XCH<sub>4</sub>) show increasing trends, with average growth rates of 2.3 and 9.5 ppb yr<sup>-1</sup>, respectively, during the  $\sim 3.5$  yr of observation. We compared the g-b FTS XCO<sub>2</sub> and XCH<sub>4</sub> data with those derived from backscattered solar spectra in the short-wavelength infrared (SWIR) region measured with Thermal And Near-infrared Sensor for carbon Observation–Fourier Transform Spectrometer (TANSO-FTS) onboard the Greenhouse gases Observing SATellite (GOSAT): NIES SWIR Level 2 products (versions 02.xx). Average differences between TANSO-FTS and g-b FTS data (TANSO-FTS minus g-b FTS) are  $0.40 \pm 2.51$  and  $-7.6 \pm 13.7$  ppb for XCO<sub>2</sub> and XCH<sub>4</sub>, respectively. Using aerosol information measured with a sky radiometer at Saga, we found that the differences between the TANSO-FTS and g-b FTS XCO<sub>2</sub> data are moderately negatively correlated with aerosol optical thickness and do not

depend explicitly on aerosol size. In addition, from several aerosol profiles measured with lidar located right by the g-b FTS, we were able to show that the presence of cirrus clouds tends to cause an overestimation in the TANSO-FTS XCO<sub>2</sub> retrieval, while high aerosol loading in the lower troposphere tends to cause an underestimation.

## 1 Introduction

Atmospheric carbon dioxide (CO<sub>2</sub>) and methane (CH<sub>4</sub>) are major greenhouse gases, the global annual mean concentrations of which have increased rapidly from 278 to 396 ppm for CO<sub>2</sub> and from 722 to 1824 ppb for CH<sub>4</sub> over the last 200 years (WMO, 2014). At present, radiative forcing of atmospheric CO<sub>2</sub> and CH<sub>4</sub> accounts for approximately 65 and 17 % of the total radiative forcing by long-lived greenhouse gases, respectively (WMO, 2014). To accurately predict future atmospheric CO<sub>2</sub> and CH<sub>4</sub> concentrations and their impact on climate, it is necessary to understand how sources and sinks of CO<sub>2</sub> and CH<sub>4</sub> are distributed around the globe and how they change over time. Although the sources and sinks can be estimated from an inversion of surface air sample/in situ measurements, column abundances are also useful in constraining emissions (Yang et al., 2007; Keppel-Aleks et al., 2012) as well as sources and sinks of CO<sub>2</sub> (Chevallier

et al., 2011). The Total Carbon Column Observing Network (TCCON) was established to derive column-averaged dry-air mole fractions of CO<sub>2</sub> and CH<sub>4</sub> (XCO<sub>2</sub> and XCH<sub>4</sub>), in addition to several other trace gases (Wunch et al., 2011a).

Global XCO<sub>2</sub> and XCH<sub>4</sub> distributions are also derived from space-based instruments: the Scanning Imaging Absorption Spectrometer for Atmospheric Chartography onboard Envisat (Bovensmann et al., 1999), the Thermal And Near-infrared Sensor for carbon Observation–Fourier Transform Spectrometer (TANSO-FTS) onboard the Greenhouse gases Observing SATellite (GOSAT) (Kuze et al., 2009), and the Orbiting Carbon Observatory-2 (XCO<sub>2</sub> only, Crisp et al., 2004; Boesch et al., 2011; Frankenberg et al., 2015). While satellite-based instruments can provide a global view, it is necessary to continuously validate these satellite products using data from instruments that have superior measurement precision and accuracy. Satellite data are validated using ground-based (g-b) high-resolution FTS data obtained from TCCON (Butz et al., 2011; Cogan et al., 2012; Guerlet et al., 2013; Morino et al., 2011; Nguyen et al., 2014; Oshchepkov et al., 2012; Reuter et al., 2011; Wunch et al., 2011b; Yoshida et al., 2013) and aircraft profile CO<sub>2</sub> and CH<sub>4</sub> data collected with instruments installed on commercial airliners and chartered aircraft (Inoue et al., 2013, 2014). Guerlet et al. (2013), however, pointed out that additional validation sites with various atmospheric and land surface conditions would be useful for improving retrieval algorithms.

We installed a high-resolution FTS instrument at Saga University (33.24° N, 130.29° E; 8 m above sea level), Japan, in June 2011, and solar spectrum measurements have been performed since the end of July 2011. This FTS is in operation following the TCCON requirements and to make a contribution to validating the satellite products. Air masses in the troposphere over Saga are dominated by transport from the Asian continent; however, depending on meteorological conditions, they may also be advected from the Pacific Ocean, especially in the summer season (Uchino et al., 2014). Because Saga and its surroundings are affected by continental aerosols and volcanic dust (Hidemori et al., 2014; Sakai et al., 2014), we also monitor aerosols with a sky radiometer and a Mie lidar, which are useful for evaluating the influence of aerosols on satellite retrievals. In the present study, we describe FTS instruments and analysis methods in Sects. 2 and 3, respectively, and present in Sect. 4 the calibration of the g-b FTS XCO<sub>2</sub> and XCH<sub>4</sub> values using aircraft measurements, time series of the g-b FTS data for the period of July 2011 to December 2014, short-term summer variations, and application of these data for validating TANSO-FTS products.

## 2 Instruments

### 2.1 Solar spectrum measurements

An FTS observation system was installed at Saga University, Japan, in June 2011. Saga is located on the Tsukushi Plane, which covers an area of 1200 km<sup>2</sup>, and is sandwiched between the Tsukushi Mountains in the north and the Ariake Sea in the south. Between 1981 and 2010, monthly mean precipitation amounts for June and July exceeded 300 mm. (<http://www.jma.go.jp/jma/indexe.html>). The city consists of cultivated land and urban areas ([http://www.biodic.go.jp/vg\\_map/vg\\_html/en/html/vg\\_map\\_frm\\_e.html](http://www.biodic.go.jp/vg_map/vg_html/en/html/vg_map_frm_e.html)).

Spectral measurements were taken with a Bruker IFS 125HR FTS instrument that has a maximum spectral resolution of 0.0035 cm<sup>-1</sup> (defined as 0.9/maximum optical path difference). The FTS is housed in a recycled 12-foot shipping container located on the grounds of Saga University. The container is insulated and equipped with an air conditioning system to keep internal temperature and humidity stable. Sunlight is directed into the container by a solar tracker (Bruker A547N), mounted on top of the container, and then introduced into the FTS by a folding mirror. The solar tracker is positioned inside a sliding dome to allow the tracker to move into every position, even in the closed state. The solar tracker features a quadrant photoelectric detector and a feedback system that enables the tracker to adjust the azimuth and elevation angles to keep solar radiation at a maximum. In order to protect the solar tracker from dust, we built a case made of polyvinyl chloride side surfaces and a top made of high-transmission glass (Asahi Glass, JFL5). To indicate the effect of the glass cover on the measured spectra and retrieved values, we show the measured spectra (Fig. S1 in the Supplement) and the retrieved XCO<sub>2</sub> values (Figs. S2 and S3) before and after the glass cover was installed. These data were acquired at the JAXA Tsukuba Space Center (36.01° N, 140.13° E), Japan, in June 2010, before the instruments were located at Saga. Figure S1 indicates that the glass cover did not cause a significant fringe pattern on the measured spectra. In the spectral range above ~ 5000 cm<sup>-1</sup>, transmittance of the glass is approximately 90 %, and the wavenumber dependence is small. Although the transmittance decreases from 90 % as the wavenumber becomes lower, spectra with a signal-to-noise ratio (SNR) of ~ 400 at 5000 cm<sup>-1</sup> can be obtained through the glass. Figures S2 and S3 indicate that a bias and degradation in XCO<sub>2</sub> were not observed and that the effect of the glass cover on the XCO<sub>2</sub> retrieval is negligibly small. The container has a precipitation sensor, allowing the sliding dome to close automatically when the sensor detects changes in conductivity due to rain and so on. An uninterruptible power supply is integrated to bridge power failures of up to 2 h.

The FTS is equipped with two room temperature detectors, an indium gallium arsenide diode (InGaAs; 4000–12 000 cm<sup>-1</sup>) and a silicon diode (Si; 9500–25 000 cm<sup>-1</sup>).

A spectral range from 3900 to 14 500 cm<sup>-1</sup> can be measured simultaneously using a dual channel acquisition mode, with a  $\sim 10\,000$  cm<sup>-1</sup> cutoff dichroic filter (Optics Balzers). In addition to the room temperature detectors, liquid nitrogen cooled indium antimonide (InSb; 1850–10 000 cm<sup>-1</sup>) and mercury cadmium telluride (MCT; 600–12 000 cm<sup>-1</sup>) detectors are installed, although their data were not used in this study. The solar absorption spectra are acquired with a spectral resolution of 0.02 cm<sup>-1</sup>, a scanner velocity of 7.5 kHz, and an aperture diameter of 1 mm. A calcium fluoride (CaF<sub>2</sub>) beam splitter is used. Two scans, one forward and one backward, are performed and individual interferograms are recorded. One measurement for a single scan takes about 110 s. The pressure inside the FTS is kept at  $\sim 0.03$  hPa with an oil-free scroll pump (Adixen, ACP15) to maintain stability of the system and to ensure clean and dry conditions.

## 2.2 Auxiliary data

A meteorological station, which consists of sensors for measuring surface pressure (Vaisala, PTB330), atmospheric temperature and relative humidity (Vaisala, HMP-155D), wind direction and speed (R. M. Young, 05103), rain amounts (Climatec, CTK-15PC), and solar and long-wave radiation (Hukseflux, RA01), is installed next to the FTS container. Solar and long-wave radiation are measured using a pyranometer and a pyrgeometer, respectively, which are part of a two-component radiation sensor. Data are recorded on a laptop computer with a frequency of 0.1 Hz through a data logger (Campbell, CR1000). Additionally, a sky radiometer, a Mie lidar, and an ozone differential absorption lidar are installed at Saga University for the purpose of validating the satellite data (Uchino et al., 2012a; Morino et al., 2013) and monitoring atmospheric aerosol and ozone.

## 2.3 Instrumental line shape (ILS) evaluation

For accurate retrievals of column abundance and/or column-averaged dry-air mole fractions, a good optical alignment of the FTS is crucial, and monitoring of the ILS is important. The monitoring of the ILS is performed by spectral measurement of an HCl gas cell (length 10 cm, diameter 4 cm, filling pressure 5 mbar) located inside the FTS instrument and by spectral analysis using the LINEFIT 14.5 software (Hase et al., 1999, 2013). Figure 1a shows time series of the modulation efficiency amplitudes at the maximum optical pass difference (OPD), which indicate deviations of the actual ILS width to that of an ideal ILS. Figure 1b shows time series of the modulation efficiency phases averaged over the entire OPD, which indicate a measure for symmetry of the ILS. The average loss in modulation efficiency amplitude at maximum OPD is  $3.0 \pm 1.2$  %, and we found that the ILS remained nearly constant during the  $\sim 3.5$  yr of operation.

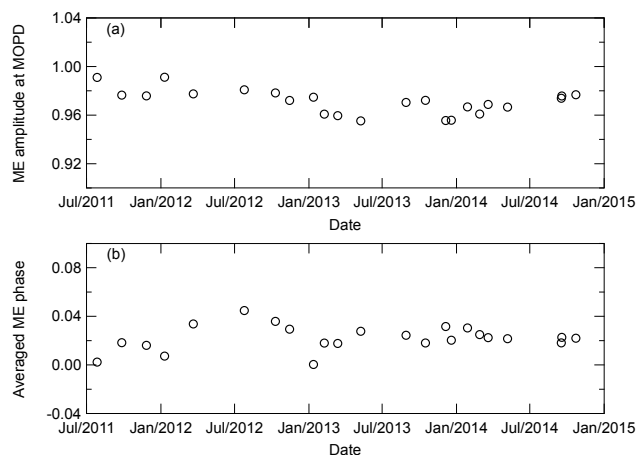


**Figure 1.** (a) Modulation efficiency amplitude at the maximum optical pass difference (OPD) and (b) modulation efficiency phase averaged over the whole OPD, which are evaluated from HCl cell spectra using the LINEFIT 14.5 software.

## 3 Analyses

### 3.1 Retrieval method

Atmospheric vertical column abundances of trace gases were derived from the measured interferograms using the latest GGG software package (GGG2014), which is used within TCCON as the common software package. We use the standard implementation of GGG for TCCON retrievals, described briefly below. Within GGG, first a solar absorption spectrum is created by performing a fast Fourier transform (FFT) of the interferogram, in which solar intensity variations caused by passing clouds and other disturbances are corrected (Keppel-Aleks et al., 2007). The spectrum is then analyzed using GFIT (a nonlinear least squares spectral fitting algorithm), in which an a priori profile is scaled to produce a synthetic spectrum that provides the best fit to the measured spectrum. From the solar absorption spectra obtained with the InGaAs detector, column abundances of CO<sub>2</sub>, CH<sub>4</sub>, CO, N<sub>2</sub>O, H<sub>2</sub>O, HDO, HF, and O<sub>2</sub> were derived. Figure 2a and b show examples of the spectral fits in the CO<sub>2</sub> and O<sub>2</sub> bands, respectively. Some large peaks of the residual (difference between the observed and the calculated spectra), especially in the CO<sub>2</sub> band, are due to discrepancies of solar lines. The XCO<sub>2</sub> value was calculated as the ratio of CO<sub>2</sub> column and dry-air column, and the dry-air column was derived from the O<sub>2</sub> column retrieved from the same spectra (i.e., O<sub>2</sub> column/0.2095). The column-averaged dry-air mole fractions of the other species were calculated in a similar fashion.

### 3.2 Screening method

In order to remove data of poor quality, we used the same screening criteria as described by Washenfelder et al. (2006), which is the standard for the TCCON data set. Among them,

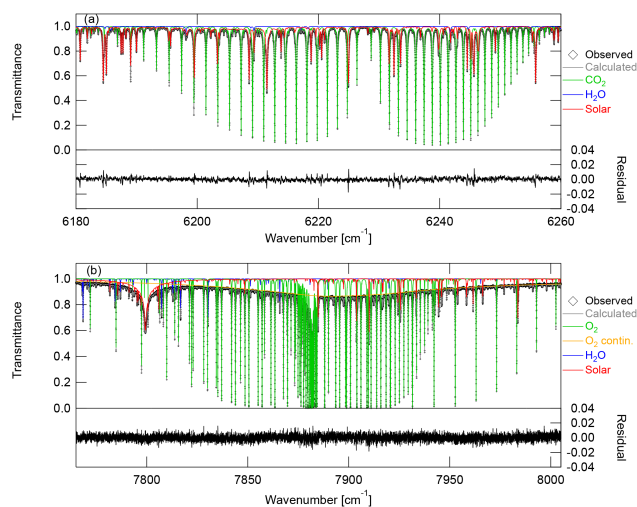


**Figure 2.** Examples of spectral fits for (a) CO<sub>2</sub> and (b) O<sub>2</sub> bands. Black diamonds denote the observed spectra on 26 November 2011, and colored lines denote the calculated spectra for the telluric and solar lines. Residuals between the observed and calculated spectra are also shown.

FTS data affected by passing clouds were filtered using the fractional variation in solar intensity during a measurement. In our case, solar intensity variations (SIV) were measured by the pyranometer with a frequency of 0.1 Hz, and data with SIV of more than 5 % were screened out. However, the measurement frequency of the pyranometer may be not high enough to capture SIV occurring around the center burst of the interferogram, which significantly impacts the Fourier-transformed spectrum. We therefore set an additional criterion as follows. We calculated average values and their standard deviations ( $1\sigma$ ) for  $\sim 1000$  data points at each side of the center burst of the interferogram. If the variability ( $1\sigma/\text{average}$ ) of the interferogram was less than 5 % at both sides, the data were considered good quality. We compared this screening method with the other one using only the interferograms, which was added to GGG2014 and adopted for several TCCON sites. Figure S4 shows the time series of XCO<sub>2</sub> for the respective screening methods, and Fig. S5 shows the numbers of data per month. From these comparisons, we found that the screening method used in the present study is conservative.

When the solar zenith angle (SZA) becomes larger than 70°, the sunlight is disturbed by the connection between the glass and the polyvinyl chloride of the solar tracker protection case. At higher angles, although solar absorption spectra can be measured through the polyvinyl chloride, the SNR values of the spectra become worse. Therefore, we adopted a criterion that the SZA has to be  $\leq 70^\circ$  rather than  $\leq 82^\circ$ , which is adopted for the typical TCCON data. The data after applying these screening criteria are available at <http://dx.doi.org/10.14291/tcon.ggg2014.saga01.R0/1149283>.

## 4 Results

### 4.1 Comparison with aircraft measurements

The g-b FTS data were corrected with TCCON common scale factors empirically determined using aircraft profiles over multiple TCCON sites to place the TCCON data on the World Meteorological Organization (WMO) standard reference scales (Wunch et al., 2010; Messerschmidt et al., 2011; Geibel et al., 2012). We compared Saga FTS data with independent aircraft profiles to ensure that the TCCON common scale factors can be applied to the Saga FTS data. Several aircraft observation campaigns in Japan were performed for calibration of the g-b FTS measurements and validation of the GOSAT products (Tanaka et al., 2012). The aircraft measurements over Saga were performed using a Beechcraft King Air 200T on 9 and 13 January 2012 and 15 January 2013. The diameter of spiral flights was less than 10 km, and maximum altitudes were approximately 7 and 10 km for the 2012 and 2013 campaigns, respectively. Instrument settings used during the aircraft measurements are described in detail in Tanaka et al. (2012). During the aircraft campaigns in 2012, CO<sub>2</sub> profiles were measured in situ with a non-dispersive infrared gas analyzer (NDIR; LI-COR, LI-840) onboard the aircraft. In addition, flask sampling was performed at eight altitude levels to check accuracy of the in situ CO<sub>2</sub> profile and to obtain other trace gas concentrations such as CH<sub>4</sub>, CO, N<sub>2</sub>O, H<sub>2</sub>, and SF<sub>6</sub>. During the aircraft campaigns in 2013, in addition to the NDIR measurements and flask sampling, alternative CO<sub>2</sub> and CH<sub>4</sub> profiles were measured in situ with cavity ring-down spectroscopy (CRDS; Picarro, G2301-m). For comparisons to the g-b FTS data, NDIR and flask data were used as aircraft profiles of CO<sub>2</sub> and CH<sub>4</sub> for 2012, respectively, while the CRDS data were used as the aircraft profiles for 2013. Note that the CO<sub>2</sub> profiles measured with NDIR and CRDS in 2013 are in agreement within  $\pm 0.2$  ppm (Tanaka et al., 2015). Precision of the aircraft data is estimated to be 0.39 ppm and 4.5 ppb for the CO<sub>2</sub> and CH<sub>4</sub> mole fractions, respectively (Tanaka et al., 2015). Figure 3a and b show the measured CO<sub>2</sub> and CH<sub>4</sub> profiles for 15 January 2013, respectively. Additional vertical profiles of pressure, temperature, relative humidity, wind direction, and wind speed were obtained by the Japan Weather Association under contract with the NIES using GPS radiosondes (Meisei Electric Co., RS-01G). Three temperature profiles measured on 15 January 2013 are shown in Fig. 3c.

Since the altitude ranges of the aircraft measurements were limited to approximately 0.5–7 or 0.5–10 km, the aircraft in situ profiles were extended below and above the flight altitude to cover the entire CO<sub>2</sub> and CH<sub>4</sub> profiles based on the assumption that the mole fractions in the boundary layer and the upper troposphere are constant against altitude. Aircraft in situ data were extrapolated to the surface using the lowest aircraft data. When aircraft measurements were not conducted up to the height of the tropopause, which was

**Table 1.** Comparison between XCO<sub>2</sub> values derived from g-b FTS and aircraft measurement. The values in the second, fourth, and fifth columns represent the results obtained using tropopause heights determined from NCEP reanalysis data and radiosonde temperature profiles (in brackets) over Saga. Aircraft data are weighted by the column averaging kernel of the g-b FTS.

Date	Tropopause height [km]	Maximum flight height [km]	FTS [ppm]	Aircraft [ppm]	$\frac{\text{FTS}-\text{Aircraft}}{\text{Aircraft}}$ [%]
9 Jan 2012	14.425 (14.333)	7.1	395.60	395.04 (395.04)	0.14 (0.14)
13 Jan 2012	15.521 (14.967)	7.0	395.17	394.51 (394.49)	0.17 (0.17)
15 Jan 2013	15.945 (8.667)	10.2	397.24	396.39 (396.72)	0.21 (0.13)

**Table 2.** Same as Table 1 but for XCH<sub>4</sub> values.

Date	Tropopause height [km]	Maximum flight height [km]	FTS [ppm]	Aircraft [ppm]	$\frac{\text{FTS}-\text{Aircraft}}{\text{Aircraft}}$ [%]
9 Jan 2012	14.425 (14.333)	7.1	1.827	1.823 (1.823)	0.22 (0.22)
13 Jan 2012	15.521 (14.967)	7.0	1.825	1.828 (1.827)	-0.16 (-0.11)
15 Jan 2013	15.945 (8.667)	10.2	1.836	1.838 (1.840)	-0.11 (-0.22)

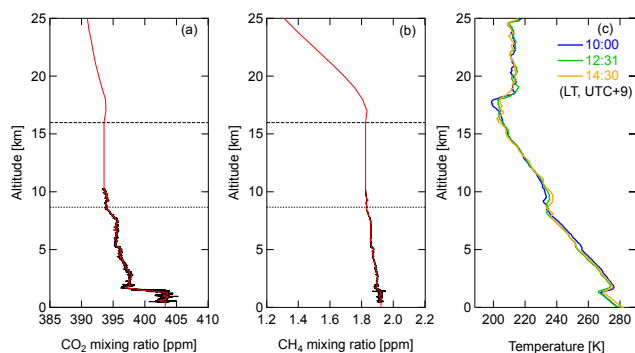


**Figure 3.** In situ (a) CO<sub>2</sub> and (b) CH<sub>4</sub> profiles measured by instruments onboard aircraft over the Saga FTS site on 15 January 2013. The black line represents the measured data and the red line is the integrated profile (see text); dashed and dotted lines indicate tropopause height determined from NCEP reanalysis data and radiosonde temperature profiles, respectively. (c) Temperature profiles measured by radiosonde launched from Saga on 15 January 2013.

determined from the NCEP reanalysis data, the highest aircraft data were extended up to tropopause height. Above the highest aircraft height or the tropopause height, GFIT a priori profiles were attached to the aircraft data. Although the tropopause height can also be obtained from radiosonde temperature data measured during the aircraft observation campaign, the tropopause height determined from the NCEP reanalysis data was used in expanding the aircraft data to the stratosphere because it was used in creating the a priori profiles. The effect of the difference in tropopause height determination is evaluated below. Completed CO<sub>2</sub> and CH<sub>4</sub> profiles are shown in Fig. 3a and b, respectively.

The XCO<sub>2</sub> values for the integrated aircraft profile were calculated according to the method of Wunch et al. (2010)

for comparison with the retrieved FTS XCO<sub>2</sub>:

$$\hat{c}_s = \gamma c_a = \left( \frac{\text{VC}_{\text{CO}_2, \text{ak}}^{\text{aircraft}} - \gamma \text{VC}_{\text{CO}_2, \text{ak}}^{\text{a priori}}}{\text{VC}_{\text{air}}} \right), \quad (1)$$

where  $c_a$  is the a priori XCO<sub>2</sub>,  $\gamma$  is the retrieved scale factor,  $\text{VC}_{\text{air}}$  is the vertical column of dry-air, and  $\text{VC}_{\text{CO}_2, \text{ak}}^{\text{aircraft}}$  and  $\text{VC}_{\text{CO}_2, \text{ak}}^{\text{a priori}}$  are vertical columns of CO<sub>2</sub> from aircraft and a priori profiles, respectively, with a column averaging kernel applied. The effect of the column averaging kernel of FTS was taken into account to equalize the sensitivities of the CO<sub>2</sub> mole fraction at each altitude for the total column. Since FTS data averaged over a time window of  $\pm 3$  h relative to the time of the aircraft measurements are compared to the aircraft data, column averaging kernels averaged over the same time window were used for the calculation. In addition, the column averaging kernels are the average of the used retrieval windows. Table 1 lists the integrated aircraft and average FTS XCO<sub>2</sub> values. The differences in XCO<sub>2</sub> between FTS and aircraft measurements are within  $\pm 0.21$ %. The differences in XCH<sub>4</sub> between the two measurements are within  $\pm 0.22$ % (Table 2). Tables 1 and 2 include results obtained using tropopause heights determined from radiosonde temperature profiles. The differences in tropopause height introduce errors of up to 0.11% in estimating aircraft XCO<sub>2</sub> and XCH<sub>4</sub> values. The error components below the maximum flight altitude were estimated by adding twice the precision of the aircraft data to the profile and re-integrating the profile (Wunch et al., 2010): 0.54 ppm for XCO<sub>2</sub> and 6.1 ppb for XCH<sub>4</sub>. The stratospheric errors in the aircraft XCO<sub>2</sub> and XCH<sub>4</sub> were estimated by shifting the a priori profile by 1 km: 0.19 ppm for XCO<sub>2</sub> and 7.1 ppb for XCH<sub>4</sub>. The total errors were calculated as the root sum squares of the three errors, and we estimated the total errors in the aircraft XCO<sub>2</sub> and

XCH<sub>4</sub> to be 0.66 ppm and 9.6 ppb, respectively. Nevertheless, since uncertainties ( $2\sigma$ ) in the TCCON common scale factor are approximately 0.2 and 0.4 % for XCO<sub>2</sub> and XCH<sub>4</sub>, respectively (Wunch et al., 2010), we find that the Saga FTS fall within this range of uncertainties and can be calibrated to the WMO standard reference scales.

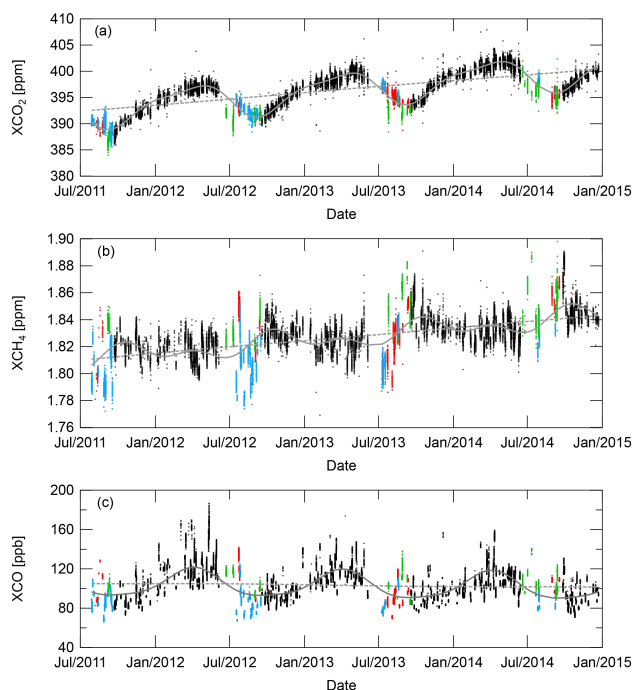
#### 4.2 Time series

Figure 4a, b, and c show time series of XCO<sub>2</sub>, XCH<sub>4</sub>, and XCO values observed at Saga during the period from July 2011 to December 2014. Both seasonal and interannual variations can be seen. We determined the seasonal and trend components in the time series using a fitting procedure described by Thoning et al. (1989), which is based on a low-pass filtering technique using FFT. Series of harmonic functions with 12- and 6-month periods were employed to represent seasonal variations, low-pass filter with a 2-year cutoff frequency was used for the long-term trend, and low-pass filter with a 150-day cutoff frequency was used for the short-term trend. The summation of the harmonic functions and the long- and short-term trends is treated as the fitting curve of XCO<sub>2</sub>. For XCH<sub>4</sub> and XCO, the summation of the harmonic functions and the long-term trend is regarded as the fitting curve. The fitting curves and the long-term trends of the retrieved values are shown in Fig. 4. Standard deviations of the differences between the retrieved values and the fitting curves are 0.81, 12.1, and 13.3 ppb for XCO<sub>2</sub>, XCH<sub>4</sub>, and XCO, respectively.

The peak-to-peak seasonal amplitude of XCO<sub>2</sub> was 6.9 ppm over Saga during July 2011 and December 2014, with a seasonal maximum and minimum in the average seasonal cycle during May and September, respectively. The long-term trend of the retrieved XCO<sub>2</sub> shows a monotonic increase. The growth rate of XCO<sub>2</sub>, which is the derivative of the long-term trend over time, is almost constant, and we obtained an average growth rate of 2.3 ppm yr<sup>-1</sup> for XCO<sub>2</sub>, similar to the global mean growth rate based on sampling measurements (WMO, 2014). The XCH<sub>4</sub> time series is characterized by large variability of XCH<sub>4</sub> during the summer season, which is discussed in the next section, as well as an increasing trend with an average growth rate of 9.5 ppb yr<sup>-1</sup>. The XCO time series has features of a seasonal cycle along with multiple peaks and a moderately decreasing trend with a growth rate of -1.0 ppb yr<sup>-1</sup>.

#### 4.3 Source of short-term variations

During the summer season, relatively low XCO<sub>2</sub> values, approximately 3–4 ppm lower than the fitting curve, were observed. As for XCH<sub>4</sub>, the observed XCO<sub>2</sub> values in the summer season indicate a larger variability compared to the other seasons. In order to investigate the causes of this variation, backward trajectory calculations were performed with the NCEP Global Data Assimilation System data using the Hy-



**Figure 4.** Time series of (a) XCO<sub>2</sub>, (b) XCH<sub>4</sub>, and (c) XCO values at Saga for the period of July 2011 to December 2014. Colors correspond to those of the trajectories for DOY 170–260 shown in Fig. 5b. Fitting curves (grey solid lines) and long-term trends (grey dashed lines) are also shown.

brid Single-Particle Lagrangian Integrated Trajectory (HYSPPLIT) model (Draxler and Rolph, 2013; Rolph, 2013). Ten-day isentropic backward trajectories were started at 2.6 km altitude (approximately 700 hPa) above the Saga FTS site. This height was selected because the change in potential temperature at 700 hPa correlates with the XCO<sub>2</sub> variation (Keppel-Aleks et al., 2012). Figure 5a and b show the results of the backward trajectories for days of year (DOY) 1–90 (January to March; winter season) and 170–260 (mid-June to mid-September; summer season), respectively. The trajectories for the summer season were classified into three types, depending on the origin of the air masses. When the start point of the trajectory was located north of 35° N and west of 145° E, the trajectories were classified as type I. When the start point of the trajectory was located south of 35° N and west of 120° E, the trajectories were classified as type II. When the start point was located anywhere else, the trajectories were classified as type III. However, provided that an air mass was located for a longer period of time west of 130° E, the trajectories were classified as type II. The trajectories for types I, II, and III relate to transport of air masses from the Asian continent (China), Southeast Asia, and the Pacific Ocean, respectively, and are colored in green (China), red (Southeast Asia), and blue (Pacific) in Fig. 5b. For the remaining days (April to mid-June and mid-September to December) not shown in Fig. 5, the transport

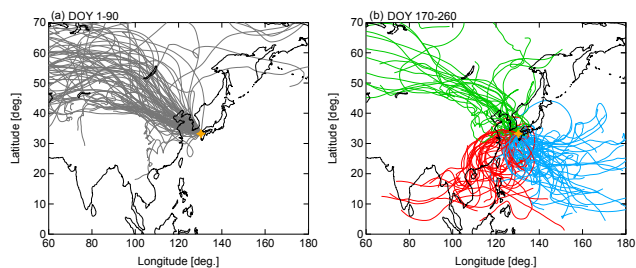


**Figure 5.** Ten-day isentropic backward trajectories from Saga at 03:00 UT on (a) DOY 1–90 and (b) DOY 170–260. The trajectories are started from an altitude of 2.6 km (approximately 700 hPa). The trajectories of DOY 170–260 are classified into three types, depending on of air mass transport, and the classification approach is described in the text. The numbers of trajectory corresponding to type I (green), type II (red), and type III (blue) are 28, 30, and 45, respectively.

from the Asian continent is dominant. Ishizawa et al. (2015) demonstrated that the XCH<sub>4</sub> variation at Saga was consistent with those obtained from the g-b FTS data at Tsukuba (36.05° N, 140.12° E) and the GOSAT TANSO-FTS data in East Chinese and Japanese areas. Additionally, on the basis of simulation output from the global atmospheric transport model of NIES (Belikov et al., 2013), they concluded that pressure pattern (i.e., wind pattern) is attributed to the XCH<sub>4</sub> variation on synoptic scale including the East Chinese and Japanese areas during the summer seasons, and this statement is consistent with the fact that, in summer 2013, the types I and II of the trajectory calculations were dominant and the larger variability of XCH<sub>4</sub> was observed at Saga.

Then, in order to derive short-term variations of XCO<sub>2</sub>, XCH<sub>4</sub>, and XCO, the respective long-term trends and seasonal cycles were subtracted from the observed values, and the residual values are referred to as  $\Delta$ XCO<sub>2</sub>,  $\Delta$ XCH<sub>4</sub>, and  $\Delta$ XCO. Figure 6a and b show correlation plots of  $\Delta$ XCO/ $\Delta$ XCO<sub>2</sub> and  $\Delta$ XCH<sub>4</sub>/ $\Delta$ XCO, respectively, whose values are represented by the daily mean values. Figures 5b and 6a indicate that most of the low-XCO<sub>2</sub> events in the summer season are driven by long-range transport of air masses associated with strong biospheric uptake over the Asian continent (type I). Wada et al. (2007) reported that low-CO<sub>2</sub> events at ground level in the summer season were observed at Minamitorishima Island (24.3° N, 154.0° E; Fig. S6) in the Northwest Pacific. We note that the air masses passing over Saga are expected to travel toward Minamitorishima Island. With regard to XCO, high-XCO events correspond to transport of air masses from the Asian continent (type I) or Southeast Asia (type II), while low-XCO events correspond to air mass transport from the Pacific Ocean (type III). Table 3 summarizes correlation coefficients and slopes of  $\Delta$ XCO/ $\Delta$ XCO<sub>2</sub> and  $\Delta$ XCH<sub>4</sub>/ $\Delta$ XCO for the different DOY and trajectory types. The negative slope of the  $\Delta$ XCO/ $\Delta$ XCO<sub>2</sub> ratio for the type I is gentler than for the

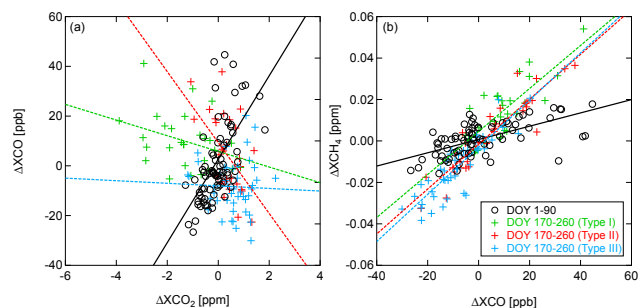


**Figure 6.** Correlation plots of (a)  $\Delta$ XCO and  $\Delta$ XCO<sub>2</sub> and (b)  $\Delta$ XCH<sub>4</sub> and  $\Delta$ XCO, which are represented by the differences between g-b FTS data and fitting curve values. Black circles are data for DOY 1–90; colored crosses are data for DOY 170–260. Colors correspond to those of the trajectories shown in Fig. 5b. Solid and dashed lines denote linear fits to DOY 1–90 and DOY 170–260 data, respectively. The linear fits to DOY 170–260 were performed separately for each trajectory type.

type II, which is due to the transport of the air masses that experienced the strong biospheric uptake of CO<sub>2</sub> over the Asian continent (i.e., stronger XCO<sub>2</sub> decreases for the type I). However, statistical *t* test indicates that the correlation for the type I as well as the type III is not significant at 95 % confidence. For the winter season, it is probable that the burning of fossil fuel causes the positive steep slope of the  $\Delta$ XCO/ $\Delta$ XCO<sub>2</sub> ratio.

As shown in Fig. 6b, the slopes of the  $\Delta$ XCH<sub>4</sub>/ $\Delta$ XCO ratio for the summer season are steeper than that for the winter season, and the differences between the types I–III for the summer season are smaller than the differences between the summer and the winter seasons. The differences in the slopes for the types I–III are statistically insignificant. The slope of the  $\Delta$ XCH<sub>4</sub>/ $\Delta$ XCO ratio for the type III is formed from the air masses with the lowest values for both  $\Delta$ XCH<sub>4</sub> and  $\Delta$ XCO, which were transported from the Pacific Ocean, where CH<sub>4</sub> and CO emissions are low. The slope of the  $\Delta$ XCH<sub>4</sub>/ $\Delta$ XCO ratio for the type II is attributable to the air masses with the highest  $\Delta$ XCH<sub>4</sub> and  $\Delta$ XCO values, which were transported from Southeast Asia, where CH<sub>4</sub> emissions from rice fields significantly increase during the summer (Bergamaschi et al., 2009) and CO concentrations are high (Worden et al., 2010). Consequently, the slopes of the  $\Delta$ XCH<sub>4</sub>/ $\Delta$ XCO ratio for the types I–III become almost equivalent. For the winter season, although the  $\Delta$ XCO values remain high, the decrease in CH<sub>4</sub> emissions over Asia during the winter causes the gentle slope of the  $\Delta$ XCH<sub>4</sub>/ $\Delta$ XCO ratio.

The  $\Delta$ XCO/ $\Delta$ XCO<sub>2</sub>,  $\Delta$ XCO/ $\Delta$ XCH<sub>4</sub>, and  $\Delta$ XCH<sub>4</sub>/ $\Delta$ XCO<sub>2</sub> ratios at Saga over the period from 2011 to 2014 were compared with  $\Delta$ CO/ $\Delta$ CO<sub>2</sub>,  $\Delta$ CO/ $\Delta$ CH<sub>4</sub>, and  $\Delta$ CH<sub>4</sub>/ $\Delta$ CO<sub>2</sub> ratios at Hateruma Island, Japan (24.05° N, 123.80° E; Fig. S6), that were derived from in situ observation over the period from 1999 to 2010 (Tohjima et

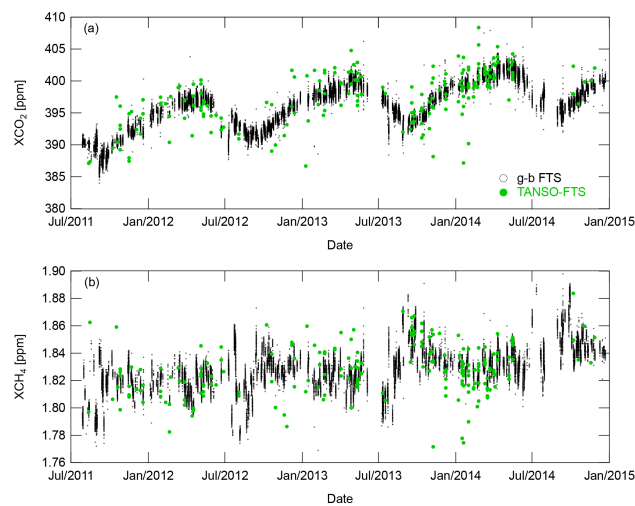
**Table 3.** Correlation coefficients and slopes of  $\Delta\text{XCO}/\Delta\text{XCO}_2$  and  $\Delta\text{XCH}_4/\Delta\text{XCO}$ . The correlation coefficients and slopes for DOY 170–260 are indicated separately for types I–III.

Period/trajectory type	$\Delta\text{XCO}/\Delta\text{XCO}_2$		$\Delta\text{XCH}_4/\Delta\text{XCO}$	
	Correlation coefficient	Slope [ppb ppm <sup>-1</sup> ]	Correlation coefficient	Slope [ppb ppm <sup>-1</sup> ]
DOY 1–90	0.62	16.6	0.91	0.84
DOY 170–260 Type I	−0.34	−3.15	0.80	1.04
DOY 170–260 Type II	−0.52	−14.3	0.92	1.08
DOY 170–260 Type III	−0.04	−0.52	0.86	1.14

al., 2014). Since the temporal and spatial distributions of CO<sub>2</sub>, CH<sub>4</sub>, and CO are attributed mainly to their emissions and following transports, the ratios among CO<sub>2</sub>, CH<sub>4</sub>, and CO derived from column observation are comparable to those derived from in situ observation (Wong et al., 2015). The  $\Delta\text{XCO}/\Delta\text{XCO}_2$ ,  $\Delta\text{XCO}/\Delta\text{XCH}_4$ , and  $\Delta\text{XCH}_4/\Delta\text{XCO}_2$  ratios for the summer season (−5.94, 0.70, and −9.40 ppb ppm<sup>-1</sup>) are comparable with the  $\Delta\text{CO}/\Delta\text{CO}_2$ ,  $\Delta\text{CO}/\Delta\text{CH}_4$ , and  $\Delta\text{CH}_4/\Delta\text{CO}_2$  ratios for the summer season in Tohjima et al. (2014), while the  $\Delta\text{XCO}/\Delta\text{XCO}_2$ ,  $\Delta\text{XCO}/\Delta\text{XCH}_4$ , and  $\Delta\text{XCH}_4/\Delta\text{XCO}_2$  ratios for the winter season (16.6, 1.19, and 7.33 ppb ppm<sup>-1</sup>) are significantly smaller than those found by Tohjima et al. (2014). Assuming that their emissions for the winter season have similar spatial distribution over East Asia, the comparison results imply that the emissions over the period from 2012 to 2014 relatively decrease in the order corresponding to CO, CH<sub>4</sub>, and CO<sub>2</sub> or increase in the order corresponding to CO<sub>2</sub>, CH<sub>4</sub>, and CO, compared to before 2010. However, since  $\Delta\text{XCO}_2/\Delta\text{XCO}$  ratios in China, which have been derived from satellite XCO<sub>2</sub> and XCO observations, differ depending on megacity (Silva et al., 2013), the differences in observed ratios at Saga and Hateruma Island might reflect the differences in regional emissions from East Asia. When the fitting procedure described in Sect. 4.2 was performed for only the type I data, the growth rates were 2.4, 8.0, and −1.9 ppb yr<sup>-1</sup> for XCO<sub>2</sub>, XCH<sub>4</sub>, and XCO, respectively. Compared to the case of using the entire data, the growth rate of XCO<sub>2</sub> increased and those of XCH<sub>4</sub> and XCO decreased. This would support the guess concerning the regional differences. In order to separate the temporal and spatial contributions to the differences in observed ratios, continuous observations and a top-down approach with high spatial resolution (e.g., Turner et al., 2015) are required.

#### 4.4 Comparisons between g-b FTS and TANSO-FTS NIES L2 data

As described in the previous section, except for transport from the Pacific Ocean during the summer season, air masses over Saga are derived from the Asian continent, where large aerosol optical depth is observed (van Donkelaar et

**Figure 7.** Time series of (a) XCO<sub>2</sub> and (b) XCH<sub>4</sub> for g-b FTS and TANSO-FTS data. Black circles are the g-b FTS data; green circles are the TANSO-FTS data within a  $\pm 2.0^\circ$  latitude/longitude rectangular area centered on the FTS site.

al., 2010). From observations of aerosols at Fukue Island ( $\sim 150$  km west-southwest of Saga, Fig. S6), the transport of continental aerosols is indicated (Hidemori et al., 2014). Therefore, the Saga g-b FTS data are believed to be appropriate for validation of the XCO<sub>2</sub> and XCH<sub>4</sub> retrievals from the satellite-borne short-wavelength infrared (SWIR) spectra in moderately aerosol-loaded scenes. We compared the g-b FTS XCO<sub>2</sub> and XCH<sub>4</sub> data with those derived from the SWIR spectra measured with TANSO-FTS onboard GOSAT. The TANSO-FTS XCO<sub>2</sub> and XCH<sub>4</sub> products used here are general public user subsets of version 02.21 (before 24 May 2014) and version 02.31 (after 16 June 2014). Figure 7a and b show a time series of XCO<sub>2</sub> and XCH<sub>4</sub> from the g-b FTS and TANSO-FTS measurements. The TANSO-FTS data are selected within a  $\pm 2.0^\circ$  latitude/longitude rectangular area centered on the FTS site, while the complete g-b FTS data are presented in those figures. The TANSO-FTS can observe seasonal variations of XCO<sub>2</sub> and XCH<sub>4</sub> similar to the g-b FTS, but the TANSO-FTS data show a higher degree of scattering than the g-b FTS data.

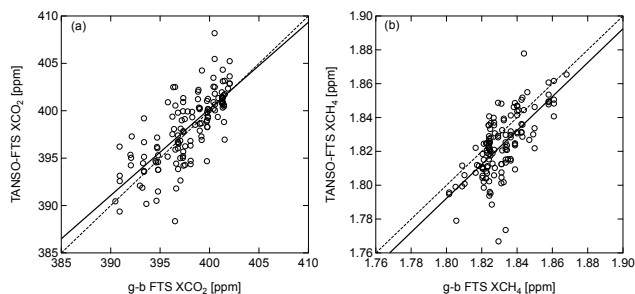


**Figure 8.** Correlation plots of (a) XCO<sub>2</sub> and (b) XCH<sub>4</sub> values derived from the g-b FTS and the TANSO-FTS spectra. The g-b FTS data within  $\pm 30$  min of the GOSAT overpass time are averaged. Solid and dashed lines denote linear fit with an intercept of 0 and 1-to-1 line, respectively.

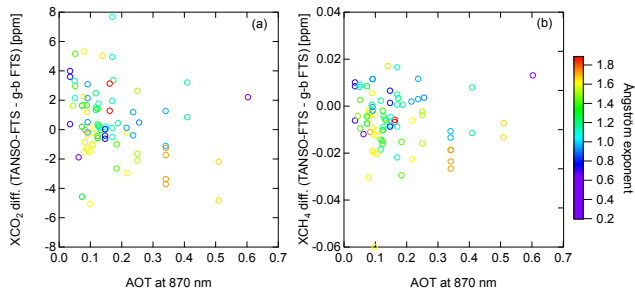
In order to accurately compare physical quantities obtained from two kinds of remote sensing instruments, it is necessary to consider the effects of differences in a priori profile and vertical resolution (i.e., column averaging kernel). First, to conform to a common a priori profile, the TANSO-FTS data were adjusted to the TCCON a priori profile (Wunch et al., 2011b). The average difference between the adjusted and the raw TANSO-FTS XCO<sub>2</sub> data (adjusted minus raw data) is  $-0.02$  ppm with a standard deviation of  $0.17$  ppm. The average difference for XCH<sub>4</sub> data is  $-4.34 \pm 0.84$  ppb. Secondly, the TCCON data were smoothed by the TANSO-FTS column averaging kernel to simulate what the TANSO-FTS would observe, provided that the TCCON data were true. The average difference between the smoothed and the raw TCCON XCO<sub>2</sub> data (smoothed minus raw data) is  $-0.08$  ppm with a standard deviation of  $0.12$  ppm. The average difference for the XCH<sub>4</sub> data is  $0.02 \pm 0.18$  ppb. We then compared the TANSO-FTS data adjusted to the TCCON a priori profile with the TCCON data smoothed by the TANSO-FTS column averaging kernel.

A correlation plot for TANSO-FTS and g-b FTS XCO<sub>2</sub> values is shown in Fig. 8a, and a correlation plot for XCH<sub>4</sub> is shown in Fig. 8b. When the g-b FTS data were collected within  $\pm 30$  min of the GOSAT overpass time (around 1325 local time), the average data and corresponding TANSO-FTS data are plotted. Therefore, the number of TANSO-FTS data in the correlation plots (Fig. 8) is less than that in the time series (Fig. 7). The average difference between TANSO-FTS XCO<sub>2</sub> values and g-b FTS data is  $0.40 \pm 2.51$  ppm (average difference  $\pm$  standard deviation). As for XCH<sub>4</sub>, the TANSO-FTS data are biased low by  $7.6$  ppb with a standard deviation of  $13.7$  ppb, compared to the g-b FTS data. The correlation coefficients amount to  $0.74$  and  $0.68$  for XCO<sub>2</sub> and XCH<sub>4</sub>, respectively. The average differences between TANSO-FTS and g-b FTS data are within the range of validation results using other TCCON site data (Yoshida et al., 2013) but with slightly larger standard deviations.

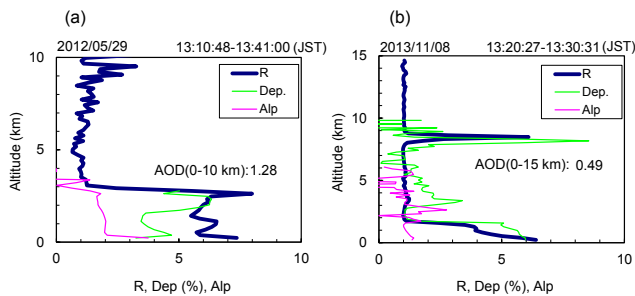
#### 4.5 Particulate effects on the TANSO-FTS NIES L2 retrievals

Figure 9a and b illustrate the differences between TANSO-FTS and g-b FTS values for XCO<sub>2</sub> and XCH<sub>4</sub> as a function of the aerosol optical thickness (AOT) values at 870 nm, which were observed with the sky radiometer (Kobayashi et al., 2006) located at Saga. We note that the AOT is here defined as the integral of the aerosol optical depth (AOD) along the entire vertical extent of the atmosphere (Bohren and Clothiaux, 2006). The match-up was limited to a  $\pm 1.0^\circ$  latitude/longitude rectangular area to highlight the local effect of aerosols on the differences between TANSO-FTS and g-b FTS data. The sky radiometer data were selected in the same manner as the g-b FTS data (i.e., average of data within  $\pm 30$  min of the GOSAT overpass time). The correlation coefficients of the difference between TANSO-FTS and g-b FTS data and the AOT values are  $-0.25$  and  $-0.07$  for XCO<sub>2</sub> and XCH<sub>4</sub>, respectively, and  $t$  values of statistical  $t$  test are  $2.4$  and  $0.66$  (the number of data point  $n = 90$ ), suggesting the correlation is significant for only XCO<sub>2</sub> at 95 % confidence. The differences between TANSO-FTS and g-b FTS data are independent of the Ångström exponent, which is a measure of the size of the aerosol particles, for both XCO<sub>2</sub> and XCH<sub>4</sub>.

Next, the effects of aerosol and cirrus profiles on the TANSO-FTS XCO<sub>2</sub> and XCH<sub>4</sub> retrievals were investigated using data measured with a lidar at Saga (Uchino et al., 2012b). The total number of coincidence measurements with the g-b FTS, TANSO-FTS, and lidar at Saga was 31. On the basis of vertical profiles of the backscattering ratio ( $R$ ) and total depolarization ratio at 532 nm (Dep.), and of the backscatter-related wavelength exponent between 532 and 1064 nm (Alp), which were measured with the lidar, we categorized the state of the atmospheric particulates (aerosol/cloud) into three types (tropospheric aerosol, cirrus cloud, and low cloud). The tropospheric aerosol was further categorized into large-AOD tropospheric aerosol and normal tropospheric aerosol (clear sky), depending on whether an AOD measured with the lidar was larger or smaller than 0.5. The numbers of the respective types resulted in 4 for the large-AOD tropospheric aerosol, 19 for the normal tropospheric aerosol, 4 for the cirrus cloud, and 4 for the low cloud. Since the low cloud scenes were likely cloudy just within the lidar receiver field of view (FOV) and was clear within the TANSO-FTS instantaneous FOV, the low cloud scenes were not treated. If only the normal tropospheric aerosol scenes were considered, the correlations of the difference between TANSO-FTS and g-b FTS data and the AOT values are not significant for XCO<sub>2</sub> as well as for XCH<sub>4</sub>. Therefore, large-AOD tropospheric aerosol and cirrus clouds would cause the negative correlation. We present distinctive case studies relevant for the large-AOD tropospheric aerosol and the cirrus cloud, and their overall impacts on the XCO<sub>2</sub> and XCH<sub>4</sub> retrievals, since there are not enough data for



**Figure 9.** (a) Differences between XCO<sub>2</sub> values derived from TANSO-FTS and g-b FTS spectra with respect to aerosol optical thickness at 870 nm measured with the sky radiometer at Saga. Color scale represents Ångström exponent derived from the sky radiometer measurements. (b) Same as Fig. 9a but for XCH<sub>4</sub> values.



**Figure 10.** Vertical profiles of the backscattering ratio (cobalt), total depolarization ratio (green), and backscatter-related wavelength exponent (pink), measured with the Mie lidar at Saga on (a) 29 May 2012 and (b) 8 November 2013.

the large-AOD tropospheric aerosol and cirrus cloud scenes to statistically show the relationship between the particulate types and the differences in XCO<sub>2</sub>/XCH<sub>4</sub> between TANSO-FTS and g-b FTS.

Figure 10a and b show vertical profiles of the backscattering ratio, the total depolarization ratio, and the backscatter-related wavelength exponent. Aerosols on 29 May 2012 in Fig. 10a were uniformly distributed below a height of 3 km and the AOD for 0–10 km was large (i.e., 1.28, assuming an aerosol extinction-to-backscatter ratio of 50 sr). For this large-AOD tropospheric aerosol scene, the differences between TANSO-FTS data closest to the Saga site and g-b FTS data are  $-4.82$  ppm for XCO<sub>2</sub> and  $-7.2$  ppb for XCH<sub>4</sub>. The mean biases for the large-AOD tropospheric aerosol scenes are  $-1.36 \pm 1.96$  ppm for XCO<sub>2</sub> and  $-9.9 \pm 7.7$  ppb for XCH<sub>4</sub>. On 8 November 2013 shown in Fig. 10b, thin cirrus clouds was observed around 8.5 km and the AOD was 0.018 assuming an aerosol extinction-to-backscatter ratio of 20 sr. Total AOD, including aerosols below 2 km was 0.49 for the altitude range of 0–15 km. The differences between TANSO-FTS data closest to the Saga site and g-b FTS data are 4.01 ppm for XCO<sub>2</sub> and 19.5 ppb for XCH<sub>4</sub>. The mean biases of XCO<sub>2</sub> and XCH<sub>4</sub> for the cirrus cloud scenes are

$2.04 \pm 2.17$  ppm and  $-1.0 \pm 12.0$  ppb, respectively. The differences between the mean biases for the large-AOD tropospheric aerosol and cirrus cloud scenes are significant for XCO<sub>2</sub> and not significant for XCH<sub>4</sub>. It is unclear what made the XCO<sub>2</sub> retrieval sensitive (or the XCH<sub>4</sub> retrieval insensitive) to the particulate type. While the difference in the spectral range practically used for the retrieval (XCO<sub>2</sub>: bands 1–3; XCH<sub>4</sub>: bands 1–2) might affect the retrieval results, further investigations are necessary to figure out the cause. As a whole, effects of aerosols/cirrus clouds on the TANSO-FTS XCO<sub>2</sub> retrievals result in a weak negative correlation of the differences between TANSO-FTS and g-b FTS data against AOT as well as in a large scatter of TANSO-FTS data. We note that the effects of the difference in aerosol type on the XCO<sub>2</sub> and XCH<sub>4</sub> retrievals would be dependent on treatment of aerosol profile in each retrieval algorithm. A treatment of cirrus clouds in the TANSO-FTS NIES XCO<sub>2</sub> and XCH<sub>4</sub> retrievals will be incorporated in the next version of the Level 2 algorithm (Y. Yoshida, personal communication, 2015).

## 5 Conclusions

Near-infrared solar absorption spectra between 3900 and 14 500 cm<sup>-1</sup> have been measured with a g-b FTS, installed at Saga, Japan. We have retrieved column-averaged dry-air mole fractions of CO<sub>2</sub>, CH<sub>4</sub>, and several other gas species from the solar absorption spectra, using the TCCON standard retrieval algorithm. From HCl gas cell measurements and analyses, we found that the ILS of the FTS was stable during its  $\sim 3.5$  yr operation. The XCO<sub>2</sub> and XCH<sub>4</sub> values derived from the g-b FTS measurements were compared with those derived from aircraft measurements. The differences between g-b FTS and aircraft data are within  $\pm 0.21$  and  $\pm 0.22$  % for XCO<sub>2</sub> and XCH<sub>4</sub>, respectively. A curve fitting procedure applied to a July 2011 to December 2014 time series of g-b FTS data, showed that the retrieved XCO<sub>2</sub> values had an average seasonal amplitude of 6.9 ppm and a growth rate of 2.3 ppm yr<sup>-1</sup>. The XCH<sub>4</sub> values indicated an increasing trend with a growth rate of 9.5 ppb yr<sup>-1</sup>, while the XCO values showed a decreasing trend with a growth rate of  $-1.0$  ppb yr<sup>-1</sup>. Based on the relationship between the deviations from the fitting curve ( $\Delta$ XCO<sub>2</sub>,  $\Delta$ XCH<sub>4</sub>, and  $\Delta$ XCO) and the back trajectory patterns, we found that the variations of XCO<sub>2</sub>, XCH<sub>4</sub>, and XCO over Saga during the summer season can be ascribed to the transport of air masses affected by biospheric activities over the Asian continent or transport of air masses from the Pacific Ocean. The steep slope of  $\Delta$ XCO/ $\Delta$ XCO<sub>2</sub> for the winter season is suggestive of air masses influenced by fossil fuel combustion. The XCO<sub>2</sub> and XCH<sub>4</sub> values derived from the g-b FTS measurements were compared with those derived from the TANSO-FTS measurements (NIES SWIR Level 2 products of version 02.xx). The average difference in XCO<sub>2</sub> between the TANSO-FTS and g-b FTS data is 0.40 ppm with a standard

deviation of 2.51 ppm. The average difference for XCH<sub>4</sub> is  $-7.6 \pm 13.7$  ppb. It is found that the differences in XCO<sub>2</sub> show a moderate negative correlation with the AOT and are independent of aerosol size. From the aerosol profiles, which were measured simultaneously with lidar at Saga, we found that TANSO-FTS XCO<sub>2</sub> data tend to be overestimated when cirrus clouds are present and underestimated in the presence of tropospheric aerosols with large optical depth. In order to clarify the effects of the difference in particulate type on the XCO<sub>2</sub> and XCH<sub>4</sub> retrievals as well as to improve the TANSO-FTS retrieval algorithm, it would in our opinion be desirable to repeat the case study presented here for different particulate types.

**The Supplement related to this article is available online at doi:10.5194/amt-8-5263-2015-supplement.**

*Acknowledgements.* We are grateful to T. Machida of the NIES for his assistance with the aircraft measurements. We also thank C. Taura of the Saga University for operation of the g-b FTS. Part of this research was supported by the Environment Research and Technology Development Fund (2A-1102) of the Ministry of the Environment, Japan. The authors gratefully acknowledge the NOAA Air Resources Laboratory (ARL) for the provision of the HYSPLIT transport and dispersion model and READY website (<http://www.ready.noaa.gov>) used in this publication.

Edited by: F. Hase

## References

- Belikov, D. A., Maksyutov, S., Sherlock, V., Aoki, S., Deutscher, N. M., Dohe, S., Griffith, D., Kyrö, E., Morino, I., Nakazawa, T., Notholt, J., Rettinger, M., Schneider, M., Sussmann, R., Toon, G. C., Wennberg, P. O., and Wunch, D.: Simulations of column-averaged CO<sub>2</sub> and CH<sub>4</sub> using the NIES TM with a hybrid sigma-isentropic ( $\sigma$ - $\theta$ ) vertical coordinate, *Atmos. Chem. Phys.*, 13, 1713–1732, doi:10.5194/acp-13-1713-2013, 2013.
- Bergamaschi, P., Frankenberg, C., Meirink, J. F., Krol, M., Viliani, M. G., Houweling, S., Dentener, F., Dlugokencky, E. J., Miller, J. B., Gatti, L. V., Engel, A., and Levin, I.: Inverse modeling of global and regional CH<sub>4</sub> emissions using SCIAMACHY satellite retrievals, *J. Geophys. Res.*, 114, D22301, doi:10.1029/2009JD012287, 2009.
- Boesch, H., Backer, D., Connor, B., Crips, D., and Miller, C.: Global characterization of CO<sub>2</sub> column retrievals from shortwave-infrared satellite observations of the Orbiting Carbon Observatory-2 mission, *Remote Sens.*, 3, 270–304, doi:10.3390/rs3020270, 2011.
- Bohren, C. F. and Clothiaux, E. E.: *Fundamentals of atmospheric radiation: an introduction with 400 problems*, Wiley-VCH, New York, 2006.
- Bovensmann, H., Burrows, J. P., Buchwitz, M., Frerick, J., Noël, S., Rozanov, V. V., Chance, K. V., and Goede, A.: SCIAMACHY – Mission objectives and measurement modes, *J. Atmos. Sci.*, 56, 127–150, doi:10.1175/1520-0469(1999)056<0127:SMOAMM>2.0.CO;2, 1999.
- Butz, A., Guerlet, S., Hasekamp, O., Schepers, D., Galli, A., Aben, I., Frankenberg, C., Hartmann, J.-M., Tran, H., Kuze, A., Keppel-Aleks, G., Toon, G., Wunch, D., Wennberg, P., Deutscher, N., Griffith, D., Macatangay, R., Messerschmidt, J., Notholt, J., and Warneke, T.: Toward accurate CO<sub>2</sub> and CH<sub>4</sub> observations from GOSAT, *Geophys. Res. Lett.*, 38, L14812, doi:10.1029/2011GL047888, 2011.
- Chevallier, F., Deutscher, N. M., Conway, T. J., Ciais, P., Ciattaglia, L., Dohe, S., Fröhlich, M., Gomez-Pelaez, A. J., Griffith, D., Hase, F., Haszpra, L., Krummer, P., Kyrö, E., Labuschagne, C., Langenfelds, R., Machida, T., Maignan, F., Matsueda, H., Morino, I., Notholt, J., Ramonet, M., Sawa, Y., Schmidt, M., Sherlock, V., Steele, P., Strong, K., Sussmann, R., Wennberg, P., Wofsy, S., Worthy, D., Wunch, D., and Zimnoch, M.: Global CO<sub>2</sub> fluxes inferred from surface air-sample measurements and from TCCON retrievals of the CO<sub>2</sub> total column, *Geophys. Res. Lett.*, 38, L24810, doi:10.1029/2011GL049899, 2011.
- Cogan, A. J., Boesch, H., Parker, R. J., Feng, L., Palmer, P. I., Blavier, J.-F. L., Deutscher, N. M., Macatangay, R., Notholt, J., Roehl, C., Warneke, T., and Wunch, D.: Atmospheric carbon dioxide retrieved from the Greenhouse gases Observing SATellite (GOSAT): Comparison with ground-based TCCON observations and GEOS-Chem model calculations, *J. Geophys. Res.*, 117, D21301, doi:10.1029/2012JD018087, 2012.
- Crisp, D., Atlas, R. M., Breon, F.-M., Brown, L.R., Burrows, J. P., Ciais, P., Connor, B. J., Doney, S. C., Fung, I. Y., Jacob, D. J., Miller, C. E., O'Brien, D., Pawson, S., Randerson, J. T., Rayner, P., Salawitch, R. J., Sander, S. P., Sen, B., Stephens, G. L., Tans, P. P., Toon, G. C., Wennberg, P. O., Wofsy, S. C., Yung, Y. L., Kuang, Z., Chudasama, B., Sprague, G., Weiss, B., Pollock, R., Kenyon, D., and Schroll, S.: The Orbiting Carbon Observatory (OCO) mission, *Adv. Space Res.*, 34, 700–709, doi:10.1016/j.asr.2003.08.062, 2004.
- Draxler, R. R. and Rolph, G. D.: HYSPLIT (HYbrid Single-Particle Lagrangian Integrated Trajectory) Model access via NOAA ARL READY Website, NOAA Air Resources Laboratory, College Park, MD, available at: <http://www.arl.noaa.gov/HYSPLIT.php>, 2013.
- Frankenberg, C., Pollock, R., Lee, R. A. M., Rosenberg, R., Blavier, J.-F., Crisp, D., O'Dell, C. W., Osterman, G. B., Roehl, C., Wennberg, P. O., and Wunch, D.: The Orbiting Carbon Observatory (OCO-2): spectrometer performance evaluation using pre-launch direct sun measurements, *Atmos. Meas. Tech.*, 8, 301–313, doi:10.5194/amt-8-301-2015, 2015.
- Geibel, M. C., Messerschmidt, J., Gerbig, C., Blumenstock, T., Chen, H., Hase, F., Kolle, O., Lavric, J. V., Notholt, J., Palm, M., Rettinger, M., Schmidt, M., Sussmann, R., Warneke, T., and Feist, D. G.: Calibration of column-averaged CH<sub>4</sub> over European TCCON FTS sites with airborne in-situ measurements, *Atmos. Chem. Phys.*, 12, 8763–8775, doi:10.5194/acp-12-8763-2012, 2012.
- Guerlet, S., Butz, A., Schepers, D., Basu, S., Hasekamp, O. P., Kuze, A., Yokota, T., Blavier, J.-F., Deutscher, N. M., Griffith, D. W., Hase, F., Kyrö, E., Morino, I., Sherlock, V., Suss-

- mann, R., Galli, A., and Aben, I.: Impact of aerosol and thin cirrus on retrieving and validating XCO<sub>2</sub> from GOSAT short-wave infrared measurements, *J. Geophys. Res.*, 118, 4887–4905, doi:10.1002/jgrd.50332, 2013.
- Hase, F., Blumenstock, T., and Paton-Walsh, C.: Analysis of the instrumental line shape of high resolution Fourier transform IR spectrometers with gas cell measurements and new retrieval software, *Appl. Optics*, 38, 3417–3422, doi:10.1364/AO.38.003417, 1999.
- Hase, F., Drouin, B. J., Roehl, C. M., Toon, G. C., Wennberg, P. O., Wunch, D., Blumenstock, T., Desmet, F., Feist, D. G., Heikkinen, P., De Mazière, M., Rettinger, M., Robinson, J., Schneider, M., Sherlock, V., Sussmann, R., Té, Y., Warneke, T., and Weinzierl, C.: Calibration of sealed HCl cells used for TCCON instrumental line shape monitoring, *Atmos. Meas. Tech.*, 6, 3527–3537, doi:10.5194/amt-6-3527-2013, 2013.
- Hidemori, T., Nakayama, T., Matsumi, Y., Kinugawa, T., Yabushita, A., Ohashi, M., Miyoshi, T., Irei, S., Takami, A., Kaneyasu, N., Yoshino, A., Suzuki, R., Yumoto, Y., and Hatakeyama, S.: Characteristics of atmospheric aerosols containing heavy metals measured on Fukue Island, Japan, *Atmos. Environ.*, 97, 447–455, doi:10.1016/j.atmosenv.2014.05.008, 2014.
- Inoue, M., Morino, I., Uchino, O., Miyamoto, Y., Yoshida, Y., Yokota, T., Machida, T., Sawa, Y., Matsueda, H., Sweeney, C., Tans, P. P., Andrews, A. E., Biraud, S. C., Tanaka, T., Kawakami, S., and Patra, P. K.: Validation of XCO<sub>2</sub> derived from SWIR spectra of GOSAT TANSO-FTS with aircraft measurement data, *Atmos. Chem. Phys.*, 13, 9771–9788, doi:10.5194/acp-13-9771-2013, 2013.
- Inoue, M., Morino, I., Uchino, O., Miyamoto, Y., Saeki, T., Yoshida, Y., Yokota, T., Sweeney, C., Tans, P. P., Biraud, S. C., Machida, T., Pittman, J. V., Kort, E. A., Tanaka, T., Kawakami, S., Sawa, Y., Tsuboi, K., and Matsueda, H.: Validation of XCH<sub>4</sub> derived from SWIR spectra of GOSAT TANSO-FTS with aircraft measurement data, *Atmos. Meas. Tech.*, 7, 2987–3005, doi:10.5194/amt-7-2987-2014, 2014.
- Ishizawa, M., Uchino, O., Morino, I., Inoue, M., Yoshida, Y., Mabuchi, K., Shirai, T., Tohjima, Y., Maksyutov, S., Ohyama, H., Kawakami, S., and Takizawa, A.: Large XCH<sub>4</sub> anomaly in summer 2013 over Northeast Asia observed by GOSAT, *Atmos. Chem. Phys. Discuss.*, 15, 24995–25020, doi:10.5194/acpd-15-24995-2015, 2015.
- Keppel-Aleks, G., Toon, G. C., Wennberg, P. O., and Deutscher, N. M.: Reducing the impact of source brightness fluctuations on spectra obtained by Fourier-transform spectrometry, *Appl. Optics*, 46, 4774–4779, doi:10.1364/AO.46.004774, 2007.
- Keppel-Aleks, G., Wennberg, P. O., Washenfelder, R. A., Wunch, D., Schneider, T., Toon, G. C., Andres, R. J., Blavier, J.-F., Connor, B., Davis, K. J., Desai, A. R., Messerschmidt, J., Notholt, J., Roehl, C. M., Sherlock, V., Stephens, B. B., Vay, S. A., and Wofsy, S. C.: The imprint of surface fluxes and transport on variations in total column carbon dioxide, *Biogeosciences*, 9, 875–891, doi:10.5194/bg-9-875-2012, 2012.
- Kobayashi, E., Uchiyama, A., Yamazaki, A., and Matsuse, K.: Application of the maximum likelihood method to the inversion algorithm for analyzing aerosol optical properties from sun and sky radiance measurements, *J. Meteorol. Soc. Jpn.*, 84, 1047–1062, 2006.
- Kuze, A., Suto, H., Nakajima, M., and Hamazaki, T.: Thermal and near infrared sensor for carbon observation Fourier transform spectrometer on the Greenhouse Gases Observing Satellite for greenhouse gases monitoring, *Appl. Opt.*, 48, 6716–6733, doi:10.1364/AO.48.006716, 2009.
- Messerschmidt, J., Geibel, M. C., Blumenstock, T., Chen, H., Deutscher, N. M., Engel, A., Feist, D. G., Gerbig, C., Gisi, M., Hase, F., Katrynski, K., Kolle, O., Lavric, J. V., Notholt, J., Palm, M., Ramonet, M., Rettinger, M., Schmidt, M., Sussmann, R., Toon, G. C., Truong, F., Warneke, T., Wennberg, P. O., Wunch, D., and Xueref-Remy, I.: Calibration of TCCON column-averaged CO<sub>2</sub>: the first aircraft campaign over European TCCON sites, *Atmos. Chem. Phys.*, 11, 10765–10777, doi:10.5194/acp-11-10765-2011, 2011.
- Morino, I., Uchino, O., Inoue, M., Yoshida, Y., Yokota, T., Wennberg, P. O., Toon, G. C., Wunch, D., Roehl, C. M., Notholt, J., Warneke, T., Messerschmidt, J., Griffith, D. W. T., Deutscher, N. M., Sherlock, V., Connor, B., Robinson, J., Sussmann, R., and Rettinger, M.: Preliminary validation of column-averaged volume mixing ratios of carbon dioxide and methane retrieved from GOSAT short-wavelength infrared spectra, *Atmos. Meas. Tech.*, 4, 1061–1076, doi:10.5194/amt-4-1061-2011, 2011.
- Morino, I., Sakai, T., Nagai, T., Uchiyama, A., Yamazaki, A., Kawakami, S., Ohyama, H., Arai, K., Okumura, H., Shibata, T., Nagahama, T., Kikuchi, N., Yoshida, Y., Liley, B., Sherlock, V., Robinson, J., Uchino, O., Yokota, T.: Impact of aerosols and cirrus clouds on the GOSAT-observed CO<sub>2</sub> and CH<sub>4</sub> inferred from ground-based lidar, skyradiometer and FTS data at prioritized observation sites, AGU Fall Meeting 2013 San Francisco, USA, 9–13 December 2013, Abstracts A21G-0152, 2013.
- Nguyen, H., Osterman, G., Wunch, D., O'Dell, C., Mandrake, L., Wennberg, P., Fisher, B., and Castano, R.: A method for collocating satellite XCO<sub>2</sub> data to ground-based data and its application to ACOS-GOSAT and TCCON, *Atmos. Meas. Tech.*, 7, 2631–2644, doi:10.5194/amt-7-2631-2014, 2014.
- Oshchepkov, S., Bril, A., Yokota, T., Morino, I., Yoshida, Y., Matsunaga, T., Belikov, D., Wunch, D., Wennberg, P. O., Toon, G. C., O'Dell, C. W., Butz, A., Guerlet, S., Cogan, A., Boesch, H., Eguchi, N., Deutscher, N. M., Griffith, D., Macatangay, R., Notholt, J., Sussmann, R., Rettinger, M., Sherlock, V., Robinson, J., Kyrö, E., Heikkinen, P., Feist, D. G., Nagahama, T., Kadyrov, N., Maksyutov, S., Uchino, O., and Watanabe, H.: Effects of atmospheric light scattering on spectroscopic observations of greenhouse gases from space: Validation of PPDF-based CO<sub>2</sub> retrievals from GOSAT, *J. Geophys. Res.*, 117, 1–18, doi:10.1002/jgrd.50146, 2012.
- Reuter, M., Bovensmann, H., Buchwitz, M., Burrows, J. P., Connor, B. J., Deutscher, N. M., Griffith, D. W. T., Heymann, J., Keppel-Aleks, G., Messerschmidt, J., Notholt, J., Petri, C., Robinson, J., Schneising, O., Sherlock, V., Velasco, V., Warneke, T., Wennberg, P. O., and Wunch, D.: Retrieval of atmospheric CO<sub>2</sub> with enhanced accuracy and precision from SCIAMACHY: Validation with FTS measurements and comparison with model results, *J. Geophys. Res.*, 116, D04301, doi:10.1029/2010JD015047, 2011.
- Rolph, G. D.: Real-time Environmental Applications and Display sYstem (READY) Website, NOAA Air Resources Laboratory, College Park, MD, available at: <http://www.ready.noaa.gov>, 2013.

- Sakai, T., Uchino, O., Morino, I., Nagai, T., Akaho, T., Kawasaki, T., Okumura, H., Arai, K., Uchiyama, A., Yamazaki, A., Matsunaga, T., and Yokota, T.: Vertical distribution and optical properties of volcanic ash from Mt. Sakurajima detected with lidar and skyradiometer over Saga, *J. Remote Sens. Soc. Japan*, 34, 197–204, doi:10.11440/rssj.34.197, 2014 (in Japanese with English abstract).
- Silva, S. J., Arellano, A. F., and Worden H.: Toward anthropogenic combustion emission constraints from space-based analysis of urban CO<sub>2</sub>/CO sensitivity, *Geophys. Res. Lett.*, 40, 4971–4976, doi:10.1002/grl.50954, 2013.
- Tanaka, T., Miyamoto, Y., Morino, I., Machida, T., Nagahama, T., Sawa, Y., Matsueda, H., Wunch, D., Kawakami, S., and Uchino, O.: Aircraft measurements of carbon dioxide and methane for the calibration of ground-based high-resolution Fourier Transform and a comparison to GOSAT data measured over Tsukuba and Moshiri, *Atmos. Meas. Tech.*, 5, 2003–2012, doi:10.5194/amt-5-2003-2012, 2012.
- Tanaka, T., Yates, E., Iraci, L., Johnson, M. S., Gore, W., Tadić, J. M., Loewenstein, M., Kuze, A., Frankenberg, C., Butz, A., and Yoshida, Y.: Two year comparison of airborne measurements of CO<sub>2</sub> and CH<sub>4</sub> with GOSAT at Railroad Valley, Nevada, *IEEE T. Geosci. Remote Sens.*, in review, 2015.
- Thoning, K. W., Tans, P. P., and Komhyr, W. D.: Atmospheric carbon dioxide at Mauna Loa Observatory: 2. Analysis of the NOAA GMCC data, *J. Geophys. Res.*, 94, 8549–8565, doi:10.1029/JD094iD06p08549, 1989.
- Tohjima, Y., Kubo, M., Minejima, C., Mukai, H., Tanimoto, H., Ganshin, A., Maksyutov, S., Katsumata, K., Machida, T., and Kita, K.: Temporal changes in the emissions of CH<sub>4</sub> and CO from China estimated from CH<sub>4</sub>/CO<sub>2</sub> and CO/CO<sub>2</sub> correlations observed at Hateruma Island, *Atmos. Chem. Phys.*, 14, 1663–1677, doi:10.5194/acp-14-1663-2014, 2014.
- Turner, A. J., Jacob, D. J., Wecht, K. J., Maasakkers, J. D., Lundgren, E., Andrews, A. E., Biraud, S. C., Boesch, H., Bowman, K. W., Deutscher, N. M., Dubey, M. K., Griffith, D. W. T., Hase, F., Kuze, A., Notholt, J., Ohyama, H., Parker, R., Payne, V. H., Sussmann, R., Sweeney, C., Velasco, V. A., Warneke, T., Wennberg, P. O., and Wunch, D.: Estimating global and North American methane emissions with high spatial resolution using GOSAT satellite data, *Atmos. Chem. Phys.*, 15, 7049–7069, doi:10.5194/acp-15-7049-2015, 2015.
- Uchino, O., Kikuchi, N., Sakai, T., Morino, I., Yoshida, Y., Nagai, T., Shimizu, A., Shibata, T., Yamazaki, A., Uchiyama, A., Kikuchi, N., Oshchepkov, S., Bril, A., and Yokota, T.: Influence of aerosols and thin cirrus clouds on the GOSAT-observed CO<sub>2</sub>: a case study over Tsukuba, *Atmos. Chem. Phys.*, 12, 3393–3404, doi:10.5194/acp-12-3393-2012, 2012a.
- Uchino, O., Sakai, T., Nagai, T., Nakamae, K., Morino, I., Arai, K., Okumura, H., Takubo, S., Kawasaki, T., Mano, Y., Matsunaga, T., and Yokota, T.: On recent (2008–2012) stratospheric aerosols observed by lidar over Japan, *Atmos. Chem. Phys.*, 12, 11975–11984, doi:10.5194/acp-12-11975-2012, 2012b.
- Uchino, O., Sakai, T., Nagai, T., Morino, I., Maki, T., Deushi, M., Shibata, K., Kajino, M., Kawasaki, T., Akaho, T., Takubo, S., Okumura, H., Arai, K., Nakazato, M., Matsunaga, T., Yokota, T., Kawakami, S., Kita, K., and Sasano, Y.: DIAL measurement of lower tropospheric ozone over Saga (33.24° N, 130.29° E), Japan, and comparison with a chemistry-climate model, *Atmos. Meas. Tech.*, 7, 1385–1394, doi:10.5194/amt-7-1385-2014, 2014.
- van Donkelaar, A., Martin, R. V., Brauer, M., Kahn, R., Levy, R., Verduzco, C., and Villeneuve, P. J.: Global estimates of ambient fine particulate matter concentrations from satellite-based aerosol optical depth: development and application, *Environ. Health Perspect.*, 118, 847–855, doi:10.1289/ehp.0901623, 2010.
- Wada, A., Sawa, Y., Matsueda, H., Taguchi, S., Murayama, S., Okubo, S., and Tsutsumi, Y.: Influence of continental air mass transport on atmospheric CO<sub>2</sub> in the western North Pacific, *J. Geophys. Res.*, 112, D07311, doi:10.1029/2006JD007552, 2007.
- Washenfelder, R. A., Toon, G. C., Blavier, J.-F., Yang, Z., Allen, N. T., Wennberg, P. O., Vay, S. A., Matross, D. M., and Daube, B. C.: Carbon dioxide column abundances at the Wisconsin Tall Tower site, *J. Geophys. Res.*, 111, D22305, doi:10.1029/2006JD007154, 2006.
- Wong, K. W., Fu, D., Pongetti, T. J., Newman, S., Kort, E. A., Duren, R., Hsu, Y.-K., Miller, C. E., Yung, Y. L., and Sander, S. P.: Mapping CH<sub>4</sub>: CO<sub>2</sub> ratios in Los Angeles with CLARIFS from Mount Wilson, California, *Atmos. Chem. Phys.*, 15, 241–252, doi:10.5194/acp-15-241-2015, 2015.
- Worden, H. M., Deeter, M. N., Edwards, D. P., Gille, J. C., Drummond, J. R., and Nédélec, P.: Observations of near-surface carbon monoxide from space using MOPITT multispectral retrievals, *J. Geophys. Res.*, 115, D16314, doi:10.1029/2010JD014242, 2010.
- World Meteorological Organization: The state of greenhouse gases in the atmosphere based on global observations through 2013, *WMO Greenhouse Gas Bulletin*, 10, 2014.
- Wunch, D., Toon, G. C., Wennberg, P. O., Wofsy, S. C., Stephens, B. B., Fischer, M. L., Uchino, O., Abshire, J. B., Bernath, P., Biraud, S. C., Blavier, J.-F. L., Boone, C., Bowman, K. P., Browell, E. V., Campos, T., Connor, B. J., Daube, B. C., Deutscher, N. M., Diao, M., Elkins, J. W., Gerbig, C., Gottlieb, E., Griffith, D. W. T., Hurst, D. F., Jiménez, R., Keppel-Aleks, G., Kort, E. A., Macatangay, R., Machida, T., Matsueda, H., Moore, F., Morino, I., Park, S., Robinson, J., Roehl, C. M., Sawa, Y., Sherlock, V., Sweeney, C., Tanaka, T., and Zondlo, M. A.: Calibration of the Total Carbon Column Observing Network using aircraft profile data, *Atmos. Meas. Tech.*, 3, 1351–1362, doi:10.5194/amt-3-1351-2010, 2010.
- Wunch, D., Toon, G. C., Blavier, J.-F. L., Washenfelder, R. A., Notholt, J., Connor, B. J., Griffith, D. W. T., Sherlock, V., and Wennberg, P. O.: The Total Carbon Column Observing Network, *Phil. Trans. R. Soc. A*, 369, 2087–2112, doi:10.1098/rsta.2010.0240, 2011a.
- Wunch, D., Wennberg, P. O., Toon, G. C., Connor, B. J., Fisher, B., Osterman, G. B., Frankenberg, C., Mandrake, L., O'Dell, C., Ahonen, P., Biraud, S. C., Castano, R., Cressie, N., Crisp, D., Deutscher, N. M., Eldering, A., Fisher, M. L., Griffith, D. W. T., Gunson, M., Heikkinen, P., Keppel-Aleks, G., Kyrö, E., Lindenmaier, R., Macatangay, R., Mendonca, J., Messerschmidt, J., Miller, C. E., Morino, I., Notholt, J., Oyafuso, F. A., Rettinger, M., Robinson, J., Roehl, C. M., Salawitch, R. J., Sherlock, V., Strong, K., Sussmann, R., Tanaka, T., Thompson, D. R., Uchino, O., Warneke, T., and Wofsy, S. C.: A method for evaluating bias in global measurements of CO<sub>2</sub> total columns from space, *Atmos. Chem. Phys.*, 11, 12317–12337, doi:10.5194/acp-11-12317-2011, 2011b.

- Yang, Z., Washenfelder, R., Keppel-Aleks, G., Krakauer, N., Randerson, J., Tans, P., Sweeney, C., and Wennberg, P.: New constraints on Northern Hemisphere growing season net flux, *Geophys. Res. Lett.*, 34, L12807, doi:10.1029/2007GL029742, 2007.
- Yoshida, Y., Kikuchi, N., Morino, I., Uchino, O., Oshchepkov, S., Bril, A., Saeki, T., Schutgens, N., Toon, G. C., Wunch, D., Roehl, C. M., Wennberg, P. O., Griffith, D. W. T., Deutscher, N. M., Warneke, T., Notholt, J., Robinson, J., Sherlock, V., Connor, B., Rettinger, M., Sussmann, R., Ahonen, P., Heikkinen, P., Kyrö, E., Mendonca, J., Strong, K., Hase, F., Dohe, S., and Yokota, T.: Improvement of the retrieval algorithm for GOSAT SWIR XCO<sub>2</sub> and XCH<sub>4</sub> and their validation using TCCON data, *Atmos. Meas. Tech.*, 6, 1533–1547, doi:10.5194/amt-6-1533-2013, 2013.